

Stabilizing effect of porosity on a flapping filament

Damiano Natali^a, Jan O. Pralits^a, Andrea Mazzino^{a,b}, Shervin Bagheri^c

^a*Università degli Studi di Genova, DICCA, via Montallegro 1, 16145 Genova, Italy*

^b*INFN and CINFAI Consortium, Genova Section, Italy*

^c*Linné Flow Centre, Department of Mechanics KTH, SE-10044 Stockholm, Sweden*

Abstract

A new way of handling, simultaneously, porosity and bending resistance of a massive filament is proposed. Our strategy extends the previous methods where porosity was taken into account in the absence of bending resistance of the structure and overcomes related numerical issues. The new strategy has been exploited to investigate how porosity affects the stability of slender elastic objects exposed to a uniform stream. To understand under which conditions porosity becomes important, we propose a simple resonance mechanism between a properly defined characteristic porous time-scale and the standard characteristic hydrodynamic time-scale. The resonance condition results in a critical value for the porosity above which porosity is important for the resulting filament flapping regime, otherwise its role can be considered of little importance. Our estimation for the critical value of the porosity is in fairly good agreement with our DNS results. The computations also allow us to quantitatively establish the stabilizing role of porosity in the flapping regimes.

Keywords: flutter, porosity, immersed boundary, drag reduction

1. Introduction

Motion of deformable, slender structures immersed in an incompressible viscous fluid is common in natural phenomena, and can be found in many applications such as paper processing [1], energy harvesting [2, 3, 4] and passive control [5, 6, 7]. In the present paper, we study numerically how porosity – a key factor in a number of both biological and technological tissues – plays a role in the dynamics of a flapping hinged filament, commonly referred to as the flag-in-the-wind problem. Similarly to previous works [8, 9,

10], an immersed boundary (IB) approach has been used in order to efficiently handle elastic interfaces interacting with a viscous incompressible fluid. The IB method is used for a wide range of applications, from blood flow around cardiac valves [11] and animal locomotion [12] to flow in deformable tubes [13].

The flag-in-the-wind – i.e. an elastic one-dimensional boundary tethered at one end in a two-dimensional laminar flow – has been studied theoretically, numerically and experimentally as the archetype for the instability of an elastic structure subject to a fluid flow. Under certain conditions a phenomenon, known as flutter, is caused by a positive feedback between the body’s deflection and the forcing exerted by the fluid flow. Often, a number of frequencies are triggered by the uniform flow affecting the body, which begins to resonate when its own natural frequency has been excited. This paper aims at investigating how porosity affects the stability of slender elastic objects exposed to a uniform stream. The long-term motion of the filament can result in a fixed-point solution, a limit-cycle flapping or a chaotic motion, depending on the governing parameters of the system [14].

Starting from Rayleigh’s first theoretical approach in 1879 [15] involving the evolution of a two-dimensional vortex sheet, the stability analyses of the flag has been enriched by inertial and structural mechanical properties [16, 17, 18, 19, 20]. More recently, increasingly accurate numerical studies (most of them using an immersed boundary approach) have come into support of analytical results [8, 21, 22, 23]. In particular, Zhu and Peskin [9] first pointed out the important role of length and mass on the onset of flapping, and described the bistable behavior of the flapping. Both Kim and Peskin [10] and Huang *et al.* [24] developed methods to handle massive filaments more efficiently. The first numerical study taking into account porosity was by Kim and Peskin [25], in which the dynamics of a porous massless 2D parachute not resisting bending was investigated. An overview of the dynamics of slender interacting body with fluid flows is found in Shelley and Zhang [14].

In the present work, we propose a way of modeling porosity and bending resistance of a massive filament which overcomes some of the major drawbacks of the method proposed in [25]. The approach proposed here is based on the method described by Huang *et al.* [24], and provides enhanced numerical stability with respect to the approach suggested in [25] by avoiding the spring-like discretization of the filament and the penetration velocity given in Eq. (15) of the same paper. The 1D porous filament can be considered as a model for the flow in one plane perpendicular to a 3D permeable sheet.

The porous filament can also be considered as a model for a three dimensional flow past an impermeable fiber, where the leakage through the porous filament corresponds to the flux past the filament in the 3D problem (see e.g. [26]).

The paper is organized as follows. Section 2 describes the numerical model, while Section 3 contains a comparison between our model for porosity and Darcy's law. In Section 4 the numerical scheme is validated using an analytical stability criterion based on the slender body theory. Numerical and theoretical results are presented in Sections 5 and 6, respectively. Finally conclusions are drawn in Section 7.

2. Problem formulation

We consider a one-dimensional incompressible elastic filament of length L^* , with mass per unit length ρ_S^* and bending rigidity K_b^* , exposed to a viscous incompressible fluid of density ρ_F^* , viscosity ν^* with a uniform velocity U_∞^* . The governing equations for the fluid are the Navier-Stokes equations (1) considered together with an appropriate volume forcing $\mathbf{f}(\mathbf{x}, t)$ to enforce the no-slip condition on the filament,

$$\begin{cases} \frac{\partial \mathbf{u}}{\partial t} + \mathbf{u} \cdot \nabla \mathbf{u} = -\nabla p + \frac{1}{Re} \nabla^2 \mathbf{u} + \mathbf{f} \\ \nabla \cdot \mathbf{u} = 0 \end{cases}, \quad (1)$$

where $\mathbf{u}(\mathbf{x}, t)$ is the velocity field, $p(\mathbf{x}, t)$ is the pressure field and Re is the Reynolds number. Here $\mathbf{x} = (x, y) \in \Omega$ is the Cartesian physical coordinates, with Ω denoting the physical domain, x and y are the stream-wise and cross-stream direction, respectively.

The filament dynamics is considered in Eqs. (2) and (3), where the first is d'Alembert elastic string equation and the second introduces the tension as a Lagrange multiplier in order to enforce incompressibility [24],

$$\frac{\partial^2 \mathbf{X}}{\partial t^2} = \frac{\partial}{\partial s} \left(T \frac{\partial \mathbf{X}}{\partial s} \right) - \frac{\partial^2}{\partial s^2} \left(\gamma \frac{\partial^2 \mathbf{X}}{\partial s^2} \right) + Fr \frac{\mathbf{g}}{g} - \mathbf{F}, \quad (2)$$

$$\frac{\partial \mathbf{X}}{\partial s} \frac{\partial^2}{\partial s^2} \left(T \frac{\partial \mathbf{X}}{\partial s} \right) = \frac{1}{2} \frac{\partial^2}{\partial t^2} \left(\frac{\partial \mathbf{X}}{\partial s} \frac{\partial \mathbf{X}}{\partial s} \right) - \frac{\partial^2 \mathbf{X}}{\partial t \partial s} \frac{\partial^2 \mathbf{X}}{\partial t \partial s} - \frac{\partial \mathbf{X}}{\partial s} \frac{\partial}{\partial s} (\mathbf{F}_b - \mathbf{F}). \quad (3)$$

Here, $s \in \Gamma$ is the Lagrangian curvilinear coordinate, with Γ denoting the body surface; $\mathbf{X}(s, t) = (X_1(s, t), X_2(s, t)) \in \Gamma$ denotes the physical position

of each material point of curvilinear coordinate s at time t and $T(s, t)$ represents the tension. In particular, on the right hand side of Eq. (2) the first two terms represent the tensional (\mathbf{F}_s) and bending terms (\mathbf{F}_b). The last term are the Lagrangian forces exerted by the fluid on the structure, obtained by means of Eqs. (4) and (6), where the first is Goldstein's feedback law [27] and the latter is the reduction due to porosity, whose meaning will be explained in Subsection 2.4. Notice that the non-slip condition is enforced implicitly by means of (4).

$$\mathbf{F}_{imp}(s, t) = \alpha \int_0^t (\mathbf{U}_{ib} - \frac{\partial \mathbf{X}}{\partial t}) dt' + \beta (\mathbf{U}_{ib} - \frac{\partial \mathbf{X}}{\partial t}), \quad (4)$$

$$\mathbf{U}_{ib}(s, t) = \int_{\Omega} \mathbf{u}(\mathbf{x}, t) \delta(\mathbf{x} - \mathbf{X}(s, t)) d\Omega, \quad (5)$$

$$\mathbf{F} = (1 - \lambda) \cdot (\mathbf{F}_{imp} \cdot \mathbf{n}) \mathbf{n} + (\mathbf{F}_{imp} \cdot \boldsymbol{\tau}) \boldsymbol{\tau}. \quad (6)$$

According to [27], α and β are negative constants chosen to enforce the no-slip condition up to arbitrary small value, λ is an overall permeability dimensionless parameter defined as the ratio between voids and total surface and \mathbf{U}_{ib} is the interpolated velocity at the Lagrangian points location. Eventually, in order to link the structural (Eqs. (2)-(3)) with the fluid part (Eq. (1)), the forcing $\mathbf{f}(\mathbf{x}, t)$ is evaluated from the Lagrangian forces by Eq. (7)

$$\mathbf{f}(\mathbf{x}, t) = \rho \int_{\Gamma} \mathbf{F}(s, t) \delta(\mathbf{x} - \mathbf{X}(s, t)) ds. \quad (7)$$

Eqs. (7) and (5) link Eulerian and Lagrangian quantities through a convolution with a discretized version of Dirac delta function δ [8]. Among a wide choice of synthetic delta functions, we make use of the one proposed by Roma [28]. Note that the difference of density scales in the dimensional version of Eqs. (1) and (2) (ρ_F^* and ρ_1^* , respectively), is taken into account in Eq. (7) through the ratio $\rho = \rho_1^*/(\rho_F^* L^*)$, see [24].

2.1. Solution Procedure

At each time step the numerical algorithm can be summarized as follows:

1. evaluation of hydrodynamical forces \mathbf{F} on the filament (Eqs. (4)-(6)) to enforce the no-slip condition up to a given value (see Subsection 2.5),
2. spreading of the force \mathbf{F} from Lagrangian points on the Eulerian grid (Eq. (7)),
3. solution of fluid flow (Eq. (1)),
4. solution of filament motion (Eqs. (2)-(3)).

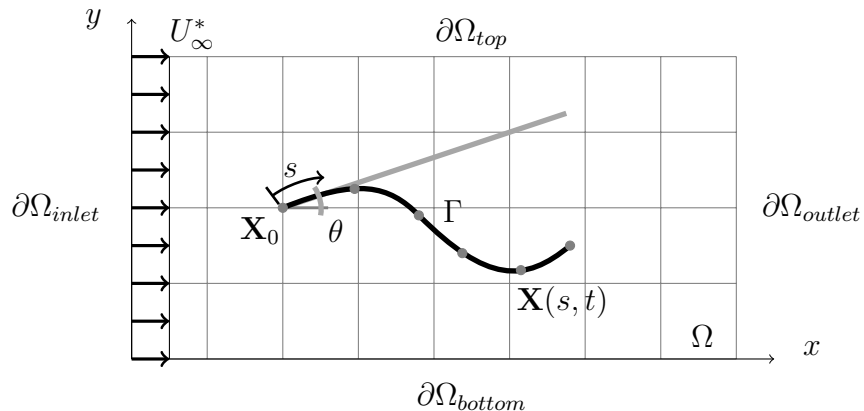


Figure 1: Filament Γ (black curve) described by a set of Lagrangian points $\mathbf{X}(s, t)$ (in gray). Initial configuration (gray line) of the filament is a straight line with a certain angle of attack θ .

2.2. Dimensionless parameters

The solution depends on the following dimensionless parameters; the Reynolds number, i.e. $Re = U_\infty^* L^* \rho_F^* / \mu^*$, the Froude number $Fr = g L^* / U_\infty^{*2}$, the bending stiffness $\gamma = K_b^* / (\rho_1^* U_\infty^{*2} L^{*2})$ and the mass ratio $\rho = \rho_1^* / (\rho_F^* L^*)$. As in [24], we also make use of the density difference $\rho_1^* = \rho_S^* - \rho_F^* A^*$, where A^* is the filament cross section area (superscript * denotes dimensional quantities). The governing equations have been made dimensionless using the filament length L^* and the free stream velocity U_∞^* . As a consequence time and pressure have been made dimensionless with L^* / U_∞^* and $\rho_F^* U_\infty^{*2}$, respectively. Furthermore, the momentum forcing \mathbf{f}^* , the Lagrangian forces \mathbf{F}^* and the tension T^* have been made dimensionless by $\rho_F^* U_\infty^{*2} / L^*$, $\rho_1^* U_\infty^{*2} / L^*$ and $\rho_1^* U_\infty^{*2}$, respectively.

2.3. Boundary conditions

Boundary conditions for Eq. (1), see Figure 1, are given by a constant velocity $\mathbf{u} = (U_\infty, 0)$ at $\partial\Omega_{inlet}$ and a convective condition $\partial\mathbf{u}/\partial t + U_\infty \partial\mathbf{u}/\partial\mathbf{n} = 0$ at $\partial\Omega_{outlet}$. We impose symmetry conditions $\{\mathbf{u} \cdot \mathbf{n} = 0$ and $\partial(\mathbf{u} \cdot \boldsymbol{\tau}) / \partial\mathbf{n} = 0\}$ on $\partial\Omega_{top}$ and $\partial\Omega_{bottom}$, where \mathbf{n} and $\boldsymbol{\tau}$ are respectively the unit vectors in the normal and tangential direction. Since the computational grid for the flow is staggered, no boundary conditions for the pressure are needed.

As already pointed out by the work by Kim and Peskin [25], pressure redistribution from higher to lower pressure zones modifies the near-wake

region behind bluff bodies, enhancing their stability.

In order to solve Eq. (2) boundary conditions are defined at both the hinged and the free end of the filament:

$$\mathbf{X}|_{s=0} = \mathbf{X}_0, \quad \left. \frac{\partial^2 \mathbf{X}}{\partial s^2} \right|_{s=0} = 0, \quad \left. \frac{\partial^2 \mathbf{X}}{\partial s^2} \right|_{s=L} = 0, \quad \left. \frac{\partial^3 \mathbf{X}}{\partial s^3} \right|_{s=L} = 0.$$

The first and second conditions enforce the filament to be hinged to the pole \mathbf{X}_0 , while the third and the fourth conditions state that the filament trailing edge is unloaded. Moreover, Eq. (3) is solved by imposing

$$\left. \frac{\partial}{\partial s} \left(T \frac{\partial \mathbf{X}}{\partial s} \right) \right|_{s=0} = -Fr \frac{\mathbf{g}}{g} + \mathbf{F}, \quad T|_{s=L} = 0,$$

where the first derives from Eq. (2) in the absence of acceleration and bending moment (hinged condition), and the second comes from the condition of an unloaded free edge.

2.4. The proposed method vs. the standard forcing approach

In order to show the difference between our proposed method and the one used in [25], we report here the Lagrangian force calculation (8) and the penetration velocity in both normal (9) and tangential (10) directions derived in [25] in order to model porosity.

$$\mathbf{F} = \mathbf{F}_s + \mathbf{F}_b = \frac{\partial}{\partial s} \left(T \frac{\partial \mathbf{X}}{\partial s} \right) - \frac{\partial^2}{\partial s^2} \left(\gamma \frac{\partial^2 \mathbf{X}}{\partial s^2} \right) \quad (8)$$

$$\left(\frac{\partial \mathbf{X}}{\partial t} - \mathbf{U} \right) \cdot \mathbf{n} = \lambda_1 (\mathbf{F} \cdot \mathbf{n}), \quad (9)$$

$$\left(\frac{\partial \mathbf{X}}{\partial t} - \mathbf{U} \right) \cdot \boldsymbol{\tau} = 0, \quad (10)$$

where λ_1 is the porosity coefficient defined in [25] as

$$\lambda = \frac{\beta \gamma}{|\partial \mathbf{X}(s, t) / \partial s|^2}, \quad (11)$$

where β is the number density of pores and γ is the aerodynamic conductance of each pore. Although the Lagrangian force \mathbf{F} is smooth, in practice – due to the IB approach used in [25]– this quantity is usually noisy. A similar lack

of smoothness is then expected in \mathbf{X} as a result of Eq. (9). Note that these equations (8-10) are not used in the this work.

The combination of Eqs. (8) and (9) generates a stiff problem – in particular due to the 4th spatial derivative in Eq. (8) – which leads to computational difficulties and numerical instabilities.

In order to overcome this limitation we undertake another approach (see Section 2), based on the IB formulation proposed in [24], whose main difference resides in the filament discretization, seen no more as a collection of springs but as a 1D structure. By doing so the noise source on the Lagrangian forcing, and thus the numerical stiffness of the problem, is removed. Similarly to [25] we also assign to the boundary an overall porosity, but rather than modeling porosity by allowing a non-zero wall-normal velocity between the boundary and the local velocity field, we reduce the normal component of momentum transferred from the fluid to an impermeable filament \mathbf{F}_{imp} to \mathbf{F} , the reduced force due to porosity (Eq. (6)). Eq. (6) is physically motivated by the fact that while tangential stresses on a solid surface arise from the tangential component of velocity normal derivative $(\partial\mathbf{u}/\partial\mathbf{n}) \cdot \boldsymbol{\tau}$, the component in the normal direction derives only from pressure differences across the surface, thus porosity affects only this component by reducing the pressure drop. We want to stress the duality of this approach with the one proposed in [25], since a relative penetration velocity will decrease the momentum transferred to the filament, while the present approach based on the reduction of momentum will lead to a penetration velocity.

2.5. Numerical approach

The computational domain is an 8×8 square ranging $[-2, 6]$ in the stream-wise direction and $[-4, 4]$ in the cross-stream direction as in [24]. The computational grid is uniform ($\Delta x = \Delta y$) in an inner region close to the hinged point $(0, 0)$ of the filament ($[-0.5, 3]$ in the stream-wise direction and $[-1, 1]$ in the cross-stream direction) with grid spacing $\Delta x = 1/75$ and stretched outside with a constant stretching ratio equal to 1.1. A convergence study on grid spacing has been performed with the smallest grid size $\Delta x = \Delta y = 1/150$ in the uniform region, showing a relative error on flapping amplitude less than 2.5%. The Lagrangian grid is made up of 150 points, so that approximately 2 Lagrangian points appear in one Eulerian cell as suggested by [10]. In order to reach a trade-off between CFL number ($\sim 10^{-2}$) and non-slip enforcement, the Goldstein's feedback law coefficients has been set $\alpha = -10$ and $\beta = -10^2$. This results in a mean flux velocity

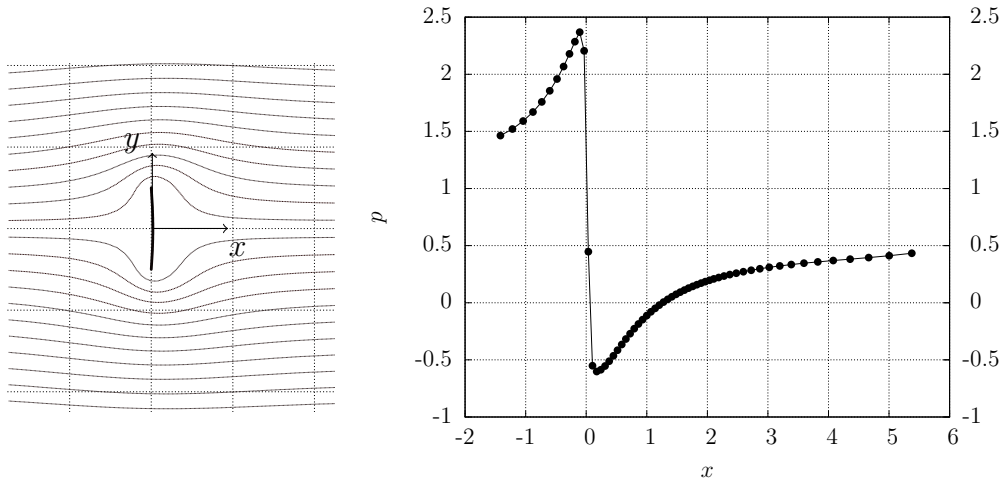


Figure 2: An inextensible membrane (left, thick solid line) simply supported at both ends is subject to a uniform flow from left (streamlines with thin solid lines) and (right) pressure profile along x . Notice the sudden pressure drop around membrane location ($x \simeq 0$) within the space of two grid points.

through the impermeable boundary normalized with the unperturbed velocity of 0.01. The initial configuration of the filament is a straight line inclined at a certain angle θ , see Figure 1.

To solve the incompressible Navier-Stokes equations we make use of the fractional step method, a projection method originally introduced independently by Chorin [29] and Temam [30] and later refined by Perot [31].

3. Comparison of the porosity model with Darcy's law

It is expected that the proposed model, accounting for porosity through the parameter λ , should capture a behavior similar to Darcy's law for porous media in the case of laminar flow at low Reynolds numbers. In this section we first derive an analytical relation between λ and the permeability coefficient k_D appearing in Darcy's law, and then we verify the obtained relation numerically by solving the governing equations outlined in Section 2.

3.1. Derivation of the $k_D - \lambda$ mapping

Darcy's law states a linear dependence between the pressure gradient ∇p and the penetration velocity of the fluid across the porous medium $\mathbf{U}_{ib} -$

$\partial\mathbf{X}/\partial t$ through the permeability coefficient k_D ,

$$\mathbf{U}_{ib} - \frac{\partial\mathbf{X}}{\partial t} = -k_D\nabla p. \quad (12)$$

By taking into account only the second term of Goldstein’s feedback law (4) as a first approximation and since $\beta \gg \alpha$, forces exerted by the fluid on the filament can be written as $\mathbf{F}_{imp} = \beta(\mathbf{U}_{ib} - \partial\mathbf{X}/\partial t)$. Since the drag on a flat plate normal to the flow is only due to the pressure difference reduced by porosity one can assume that

$$\frac{\mathbf{F}_{imp}(1 - \lambda)}{\delta} \sim \frac{\partial p}{\partial x}, \quad (13)$$

where δ is the width of the membrane, given by the “effective radius” of the Dirac delta function used by the IB method. Here, δ has been estimated to be twice the minimum grid spacing, i.e. $\delta = 2\Delta x_{min} = 2\Delta y_{min}$. Finally one obtains

$$k_D = -\frac{\delta}{\beta(1 - \lambda)}. \quad (14)$$

This analytical model is compared with the numerical solution in Section 3.2.

3.2. Validation with Darcy’s law

Several simulations have been performed by considering a porous membrane hinged at both ends perpendicular to an incoming uniform flow, see Figure 2. Different values of λ and four different Reynolds number (2.5, 5, 7.5, 10) are considered ($Fr = 0$). By sampling the pressure immediately upstream and downstream of the membrane along the x -axis we obtain the pressure gradient across the membrane, see Figure 2, while flow measurements are computed by interpolating the fluid velocity on the membrane. The linear relationship between the pressure gradient across the membrane and the fluid flux ϕ computed as linear integral of the penetration velocity between the fluid and the solid, is in good agreement with Darcy’s law at the Reynolds numbers under investigation, see Figure 3. Darcy’s parameter k_D for each value of λ is thus obtained through a linear regression of the simulation results, leading to a numerical mapping curve ($\lambda - k_D$). Figure 3 shows an excellent agreement between the numerical results and the analytical prediction from equation (14).

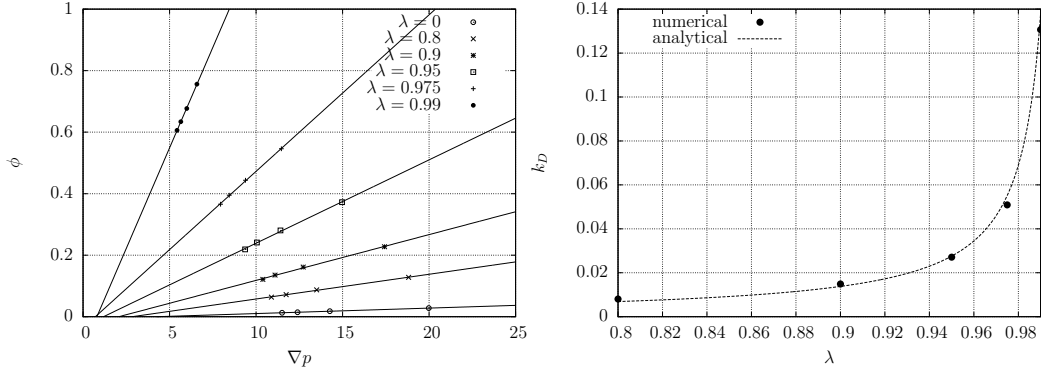


Figure 3: Flux ϕ as a function of the pressure gradient ∇p for $Re = 2.5, 5, 7.5, 10$, $Fr = 0$ and different values of λ (left). For each λ a linear regression has been performed (solid lines) in order to obtain Darcy's porosity coefficient k_D , which is given by the slope of each line. Comparison between analytical prediction for k_D , eq. (14), and numerical results (right).

4. Validation of the impermeable filament

Before focusing on porous filaments, we validate our numerical scheme against results available in the literature. In particular the analytical results in [16] has been taken as a reference for all numerical simulations. This model considers the beam equation with external loads given by the slender body theory [32], resulting in following the dispersion relation

$$(\rho + \rho_a)(1.3Re^{-1/2} + \gamma k^2) - \rho\rho_a \geq 0, \quad (15)$$

where $\rho_a = 2/k$ from potential theory [18]. Here, the following non-dimensional quantities have been introduced,

$$\rho = \frac{\rho_s^*}{\rho_f^* L^*}, \quad \gamma = \frac{K_b^*}{\rho_f^* U^{*2} L^{*3}},$$

where ρ_s^* is the structure linear density, ρ_f^* is the fluid density and k is the wavenumber associated with the flapping. We would like to point out that the definition of ρ and γ used in Eq. (15) differs from that given in Section 2; Eq. (15) derives from the dynamical beam equation considering the absolute beam density ρ_s^* in the inertial term and not the density difference ρ_1^* as required by the immersed boundary approach.

In the numerical results shown from here on the Reynolds number has been set to $Re = 200$ and the Froude number to $Fr = 0$. The bifurcation

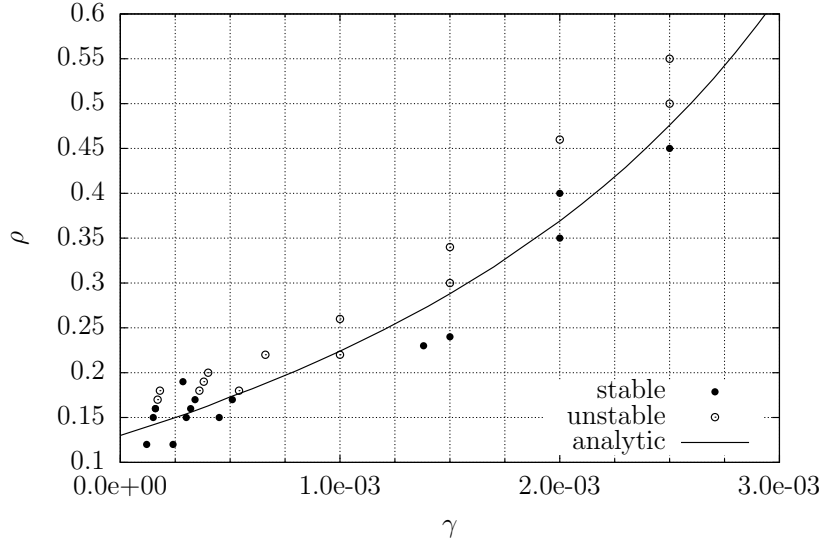


Figure 4: Comparison between analytical models and DNS simulations for $Re = 200$ and different values of ρ and γ .

line between stable and unstable solutions has been investigated numerically for different values of ρ and γ and the results are presented in Figure 4. The limit-cycle solutions are indicated with open circles while stable solutions (straight filament aligned with the main stream) are shown with filled circles. The solution of Eq. (15), as given by Connel and Yue [16], is shown with a solid line. The numerical and analytical results are in good agreement when $\gamma < 2.5 \cdot 10^{-3}$, which coincides with the range of values investigated in [16]. Above this critical value of the bending stiffness the agreement deteriorates. In Appendix A, we present a possible explanation based on a change of the flapping filament shape for $\gamma > 2.5 \cdot 10^{-3}$. This results in a modification of the added mass coefficient (from potential theory).

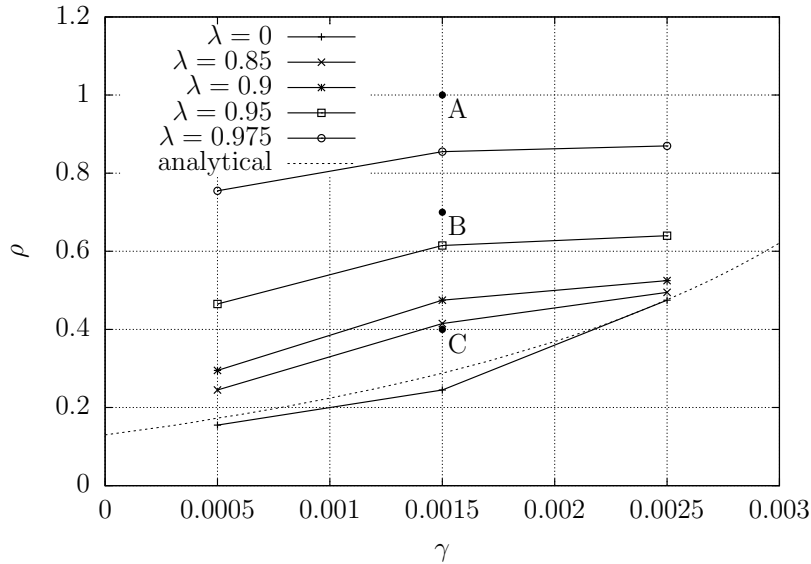


Figure 5: Neutral curve on the plane (γ, ρ) for $Re = 200$, $Fr = 0$ and $\lambda = 0$ obtained numerically. The analytical curve for $\lambda = 0$ is taken from [16] and shown with a dotted line, whereas the solid lines with symbols represent neutral curves for different porosity.

5. Numerical results

5.1. Porous filament

In order to assess the stabilizing property of porosity, several numerical simulations with different values of the parameters (γ, ρ) have been performed at $Re = 200$, $Fr = 0$ and for different values of the porosity λ . For the impermeable case ($\lambda = 0$), we compare the numerical results with the analytical curve obtaining a close agreement, which can be seen in Figure 5. When porosity is considered ($\lambda \neq 0$), the critical density difference ρ increases with λ for a given value of bending stiffness γ . This means that an increasingly porous filament requires an higher density in order to experience sustained flapping.

We consider three different configurations in the (γ, ρ) plane (marked with bullets A, B and C in Figure 5). Table 1 reports the critical values of porosity $\lambda_{c,n}$ for which the flapping behavior changes from unstable to stable. As observed in Figures 6 and 7, an increased porosity results in a reduction of both the peak-to-peak amplitude and frequency even for $\lambda < \lambda_{c,n}$, i.e. in

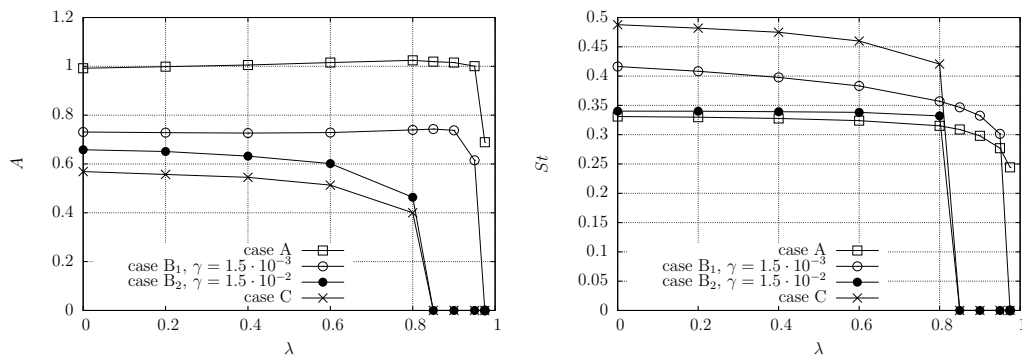


Figure 6: Peak-to-peak oscillation amplitude and flapping Strouhal number as function of porosity. Each curve is drawn for different sets of parameters (γ, ρ) , see Figure 5.

the sustained flapping regime.

	γ	ρ	$\lambda_{c,n}$
A	$1.5 \cdot 10^{-3}$	1.0	0.975
B ₁	$1.5 \cdot 10^{-3}$	0.7	0.95
B ₂	$1.5 \cdot 10^{-2}$	0.7	0.85
C	$1.5 \cdot 10^{-3}$	0.4	0.85

Table 1: Values of bending stiffness γ and mass ratio ρ for bullets A, B and C in Figure 5. A stable configuration (i.e. no flapping) is obtained numerically when $\lambda > \lambda_{c,n}$.

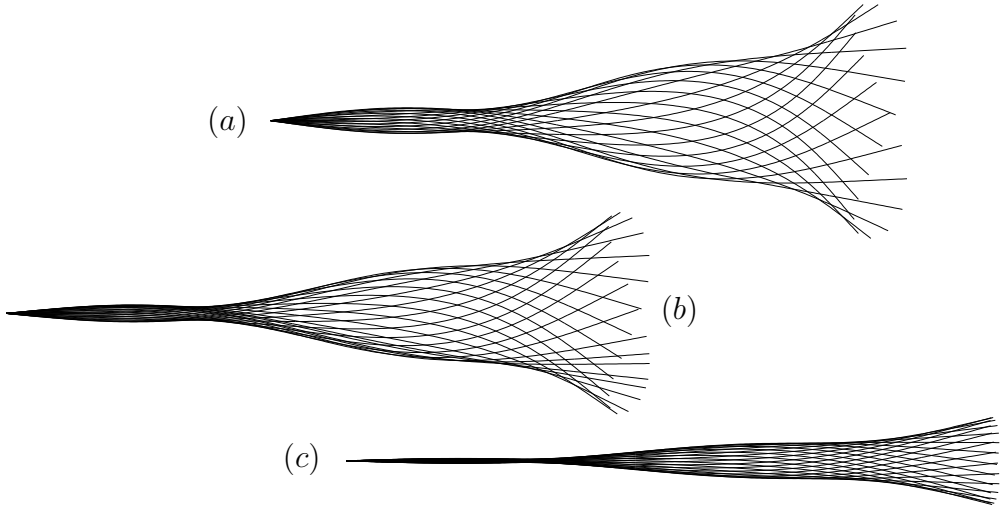


Figure 7: Snapshots of porous filaments ((a) $\lambda = 0$, (b) $\lambda = 0.6$, (c) $\lambda = 0.8$) during one flapping cycle (case C, Figure 5 and 6).

Besides kinematics, the effects of porosity on the time behavior of the forces acting on the flapping filament have also been assessed. Both maximum values of lift and drag forces decrease monotonically as porosity increases (Figure 9, left) with a weaker effect on the drag than on the lift force. This is in agreement with the role of porosity on the pressure distribution around the filament. By allowing normal-to-filament velocities to arise, porosity reduces pressure differences across the filament reducing lift and, consequently, flapping amplitude as clearly observed in Figure 7. On the other hand, assuming that pressure drag is the leading contribution, the effect of porosity on the drag force is weaker than on the lift force. The filament indeed flaps more or less aligned with the unperturbed flow, i.e. normal to the direction along which pressure gradient reduces. The effects of porosity on lift and drag yield to an optimal value of $\lambda \simeq 0.6$ for which the lift-to-drag ratio is maximized (Figure 9, right).

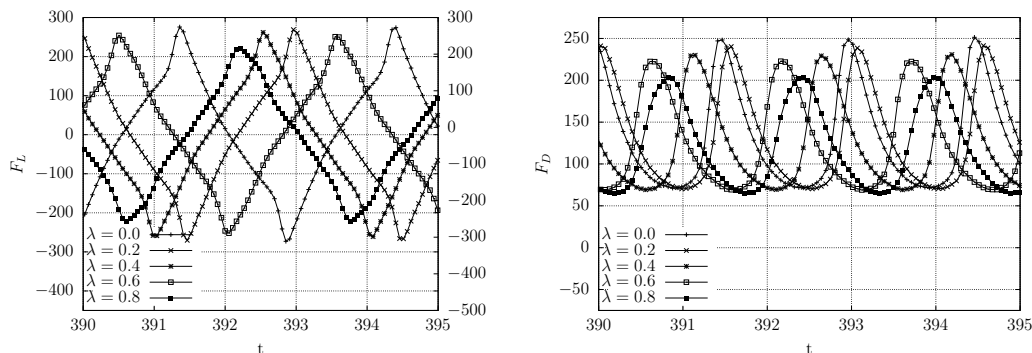


Figure 8: Time evolution of the lift (left) and drag forces (right) for case C (see Figure 5).

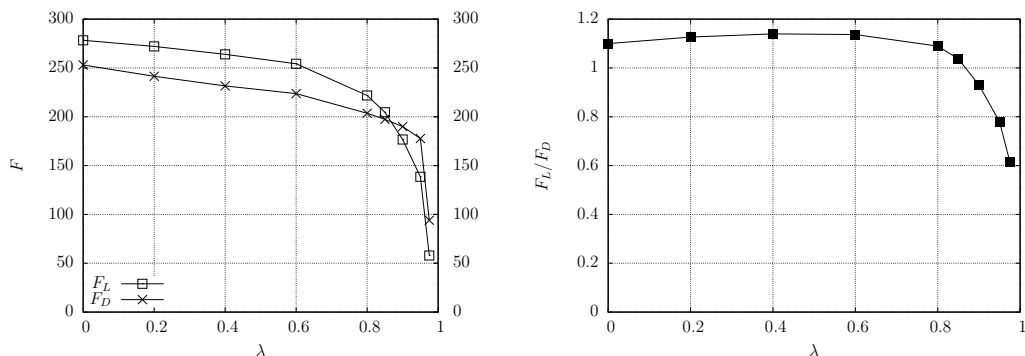


Figure 9: Maximum values of lift and drag forces (left) and lift-to-drag ratio (right) for case C (see Figure 5), all as a function of the porosity.

6. Time-scale investigation

In previous sections we have shown quantitative results on the stabilization of elastic filament due to porosity. In this section we provide a simple physical mechanism at the origin of stabilization and show that the phenomenon can be traced back to a resonance condition between porous and hydrodynamical time scales.

Physical mechanisms at work may interact stronger when their characteristic time-scales are of the same order of magnitude. Arguments of this type have been successful, e.g., to explain symmetry breaking mechanism in fluid-structure interaction [33] as well as emergence of elastic instabilities [19, 4], the emergence of macroscopic spatial scales at which microscopic polymers cause viscoelastic behavior [34]. In this spirit, we define the dimensional

porous time as the characteristic time needed by mass to cross the membrane of thickness δ . Following Darcy's empirical law $\mathbf{U}_{ib}^* - \partial \mathbf{X}^* / \partial t^* = -k \nabla p^*$, we estimate this quantity to be:

$$\tau_{por}^* = \frac{\delta^*}{\|\mathbf{U}_{ib}^* - \partial \mathbf{X}^* / \partial t^*\|} = \frac{\delta}{k \nabla p^*} = \frac{\delta^2}{k \Delta p^*}. \quad (16)$$

In order to give a quantitative value for the pressure difference across the membrane, we resort to the dimensional version of slender body theory [17] already used in [16, 18]

$$\Delta p^* = m_a^* \left(\frac{\partial}{\partial t^*} + U_\infty^* \frac{\partial}{\partial s^*} \right)^2 h^* \simeq m_a^* \left(\frac{U_\infty^*}{L^*} \right)^2 h^*, \quad (17)$$

where m_a^* is the added mass, $(\partial/\partial t^* + U_\infty^* \partial/\partial s^*)$ is the convective derivative for a fluid particle near the filament and h^* is the vertical displacement. From potential flow solution $m_a^* = (2/k) \rho_a^* L^*$, where k is oscillation wavenumber. Inserting (14) and (17) into (16) one obtains

$$\tau_{por}^* = - \frac{\delta^* L^{*2} \beta^* (1 - \lambda)}{m_a^* U_\infty^{*2} h^*}.$$

Physically, this is the time it takes for the flow to reduce the pressure difference Δp^* across the filament.

Our aim here is to compare this characteristic time-scale with the hydrodynamical time-scale, roughly estimated as $\tau_{hdr}^* = L^*/U_\infty^*$, in order to assess the critical value of λ in order to have resonance between porosity and hydrodynamics. The ratio between the two time scale is written

$$\frac{\tau_{por}^*}{\tau_{hdr}^*} = - \frac{\delta^* L^{*2} \beta^* (1 - \lambda) U_\infty^*}{m_a^* U_\infty^{*2} h^*} \frac{U_\infty^*}{L^*} = - \frac{\delta^* L^* \beta^* (1 - \lambda)}{m_a^* U_\infty^* h^*} \simeq 1. \quad (18)$$

From expression (18) we can derive a theoretical critical value $\lambda_{c,t}$, that written in dimensionless form reads

$$\lambda_{c,t} \simeq 1 + \frac{\rho_a h}{\delta \beta}. \quad (19)$$

If we use the parameters given in Table 2 we obtain theoretical critical value of λ in good agreement with the direct numerical simulations. Interestingly, this result shows that the stabilizing effect of porosity occurs when we are very close to $\lambda = 1$, in qualitative agreement with what one can observe from DNS (see Table 1).

	γ	k	ρ_a	h	δ	β	$\lambda_{c,t}$	k_D
B ₁	$1.5 \cdot 10^{-3}$	2π	$1/\pi$	0.73	2/75	-10^2	0.91	$2.96 \cdot 10^{-3}$
B ₂	$1.5 \cdot 10^{-2}$	π	$2/\pi$	0.66	2/75	-10^2	0.84	$1.67 \cdot 10^{-3}$

Table 2: Values of parameters entering in Eq. (19) with the corresponding critical theoretical value of λ and Darcy’s parameter k_D . ρ_a has been set equal to $2/k$ in accordance with potential theory [18], while $\delta = 2\Delta x_{min}$. For vertical displacement h the peak-to-peak amplitude at $\lambda = 0$ has been considered. Note that, as shown in Appendix Appendix A, the oscillation wavenumber k is function of the bending stiffness γ .

7. Conclusions

We propose a novel way of handling simultaneously porosity and bending resistance of a massive filament which extends previous methods where porosity was taken into account in the absence of bending resistance of the structure. Moreover, our numerical strategy overcomes numerical stability issues by avoiding the formulation given in [25] involving the Lagrangian forces \mathbf{F} . The newly designed algorithm has been exploited to investigate how porosity affects the stability of slender elastic objects exposed to a uniform stream.

First we validate our numerical code by neglecting porosity and comparing numerical results against predictions from an existing analytical model [16] where the hydrodynamical forces on the filament are described by the “slender body theory” [32]. As a side result, in Appendix A we find a critical bending stiffness above which the critical density ratio increases with the bending stiffness at much smaller rate than what predicted in [16]. We also propose a simple way to extend the analytical model to account for that. It is left for future research the detailed analysis of the remaining discrepancies.

In the case of porosity we first derive and verify a relation between our free model parameter λ and the porosity parameter k_D appearing in Darcy’s law. From modeling arguments it is found that $k_D \propto (1 - \lambda)^{-1}$, in excellent agreement with the numerical simulations at low Reynolds number.

We also investigate how porosity modifies the stability properties of filaments hinged in uniform flow fields. It is found that porosity effectively increases the stability zone only when the porosity parameter λ is greater than a critical value λ_c . The existence of a critical porosity λ_c is confirmed also by the numerical simulations of porous filaments undergoing sustained flapping, for which both flapping amplitude and frequency drop for $\lambda > \lambda_c$.

L^*	$1 \cdot 10^{-2}$	m
ρ_S^*	$2.2 \cdot 10^{-5}$	kg/m
ρ_F^*	$5 \cdot 10^{-3}$	kg/m^2
ρ_1^*	$2.19 \cdot 10^{-5}$	kg/m
A^*	$2 \cdot 10^{-5}$	m
K_b^*	$4.67 \cdot 10^{-10}$	Nm^2
U^*	2.92	m/s

Table 3: Values of experimental parameters obtained using polyethylene ($\rho = 1100 \text{ kg/m}^3$, $E = 7 \cdot 10^8 \text{ N/m}^2$) extruded by 1 mm in a water soap film ($\rho = 1000 \text{ kg/m}^3$) having thickness $5 \text{ }\mu\text{m}$.

In order to give a physical explanation for this we propose a simple resonance mechanism between a characteristic porous time-scale and the standard characteristic hydrodynamic time-scale. The resonance condition fixes a critical value above which porosity affects the resulting filament flapping regime, while if below its role can be considered of little importance. The estimation for the critical value of the porosity is in qualitative agreement with our DNS results. Finally, we observed reduction of both lift and drag forces induced by porosity, ascribing it to the penetration velocity that reduces the pressure difference between the two sides of the structure, and find an optimum value of λ that maximizes the lift-to-drag ratio.

In Appendix B we present a trivial generalization of the model by Connel and Yue [16] to account for porosity which captures the stability effect induced by porosity qualitatively.

We conclude with a suggestion of a possible experimental set-up to realize the same conditions we simulate in our 2-D case ($\rho = 0.438$, $\gamma = 0.025$). In particular we consider the experiment to be carried out in a soap-film facility (see e.g. [35]) with soap film thickness and solid extrusion as reported in Table 3. In order to achieve the values of λ used in this work one needs a grid made up of fibers interspaced by ~ 100 times their characteristic diameter.

8. Acknowledgements

A.M. and J.O.P. thank the financial support from the PRIN 2012 project n. D38C1300061000 funded by the Italian Ministry of Education. We also thank the financial support for the computational infrastructure from the

Italian flagship project RITMARE. S.B. acknowledges the support of the Swedish Research Council (VR-2010-3910) and the Göran Gustafsson Foundation. Discussions and suggestions with Hamid Kellay are also kindly acknowledged.

Appendix A. Impermeable filament dynamics for higher bending stiffness

Figure A.10 shows the numerical results of Eq. (15) for γ up to $5 \cdot 10^{-2}$. The analytical solution given by Connel and Yue [16] is shown with a solid line. The numerical and analytical results are in good agreement when $\gamma < 2.5 \cdot 10^{-3}$, which coincides with the range of values investigated by Connel and Yue [16]. Above this critical value of the bending stiffness the agreement deteriorates.

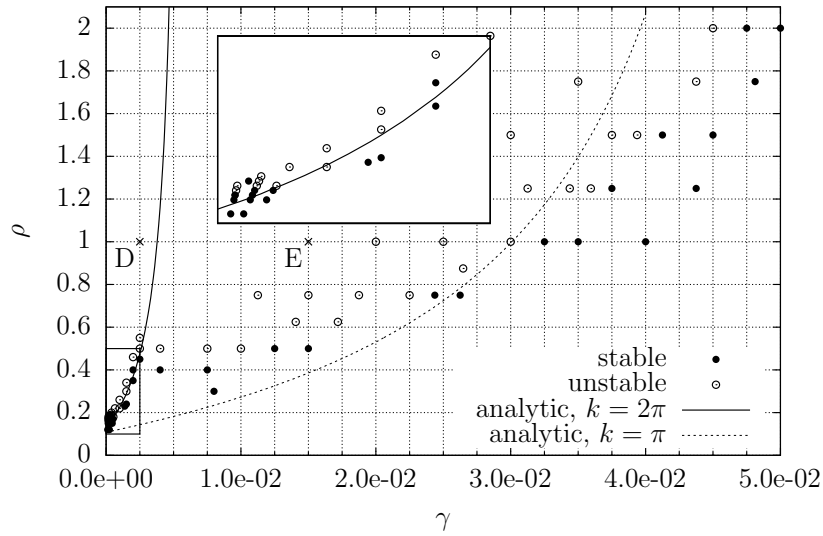


Figure A.10: Comparison between analytical models and DNS simulations for $Re = 200$, $Fr = 0$ and different values of ρ and γ . The close-up refers to the rectangle near the axis origin.

This discrepancy can partly be explained by a modification of the filament shape as the value of γ exceeds $2.5 \cdot 10^{-3}$. In relation to Figure A.10, Figure A.11 depicts snapshots of the filament during a flapping cycle for two

different values of γ , whereas in Figure A.12 the time evolution of the trailing edge cross-stream coordinate is shown (cases D and E in Figure A.10, respectively). Vorticity iso-contours for the same parameter sets can be seen in Figure A.13.

By inspection of Figure A.11 it can be noted that the wavenumber of the filament shape is approximately $k = 2\pi$ for $\gamma < 2.5 \cdot 10^{-3}$, while k is more close to π when $\gamma > 2.5 \cdot 10^{-3}$. Following the derivation of the model, this shape alteration leads to a variation of the added mass coefficient obtained from potential theory. The new curve drawn for $k = \pi$ matches qualitatively the DNS simulations, see dotted curve in Figure A.10. An additional discrepancy between analytics and numerics may be due to the rough assumption of approximating the filament tension as the one obtained by a stationary and laminar boundary layer, Blasius, flow along its whole length.

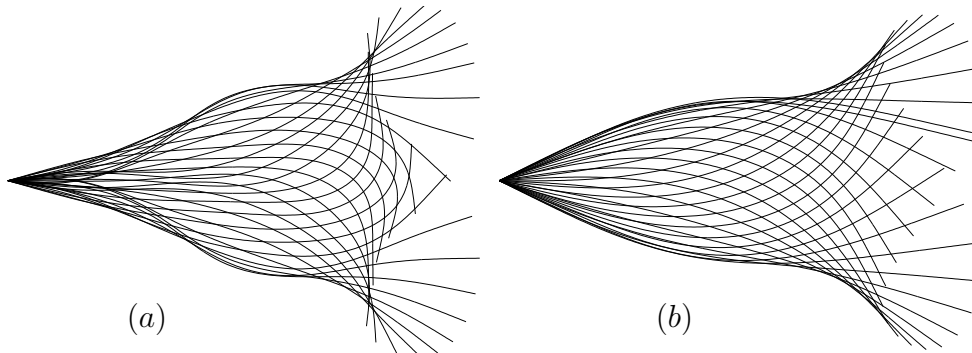


Figure A.11: Snapshots of impermeable filament during one flapping cycle for case D (a) and E (b) depicted on Figure A.10. While a unique concavity characterizes the behavior of the right filament, an inflection point is clearly visible in the left filament.

Appendix B. Straightforward generalization of the analytical model to account for porosity

Let us perform a stability analysis study on a simplified model inspired from the work by [16]. Porosity reduces the force exerted in the normal direction by the fluid on the filament by allowing a mass transfer, thus reducing the pressure difference across the boundary.

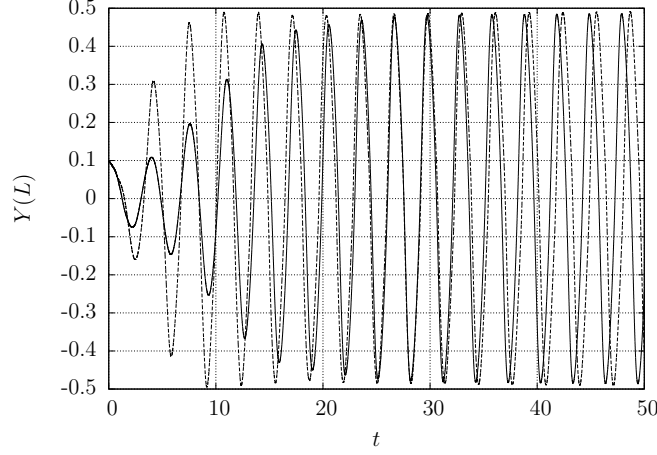


Figure A.12: Y-coordinate of the filament trailing edge in the impermeable cases D (solid line) and E (dashed line) depicted on Figure A.10.

In order to account for the porosity effects we propose to reduce the hydrodynamical forces by a factor $(1 - \lambda)$

$$L(x, t) = -\rho_a(1 - \lambda)\left(\frac{\partial}{\partial t} + U\frac{\partial}{\partial x}\right)^2 h$$

from which

$$[\rho + (1 - \lambda)\rho_a]\frac{\partial^2 h}{\partial t^2} + 2\rho_a(1 - \lambda)\frac{\partial}{\partial x}\frac{\partial h}{\partial t} + [\rho_a(1 - \lambda) - \tau]\frac{\partial^2 h}{\partial x^2} + \gamma\frac{\partial^4 h}{\partial x^4} = 0$$

by using the same scaling as in Section 4 and where λ represents porosity. Again, $\lambda = 0$ reduces to the impermeable case and $\lambda = 1$ is the limit for an infinitely porous filament. If we now perform a stability analysis, we end up with a slightly different stability condition

$$\left[\frac{2(1 - \lambda)}{k} + \rho\right] \left[\gamma k^2 + \frac{1.3}{\rho\sqrt{Re}}\right] - \frac{2(1 - \lambda)}{k} \geq 0, \quad (\text{B.1})$$

from which it is possible to derive critical values for linear density, flexural stiffness and incoming velocity related to porosity λ and Reynolds number Re . Results of the analytical neutral stability curves are presented in Figure B.14 for $Re = 200$ and $Fr = 0$ in the plane (ρ, γ) for different values of λ .

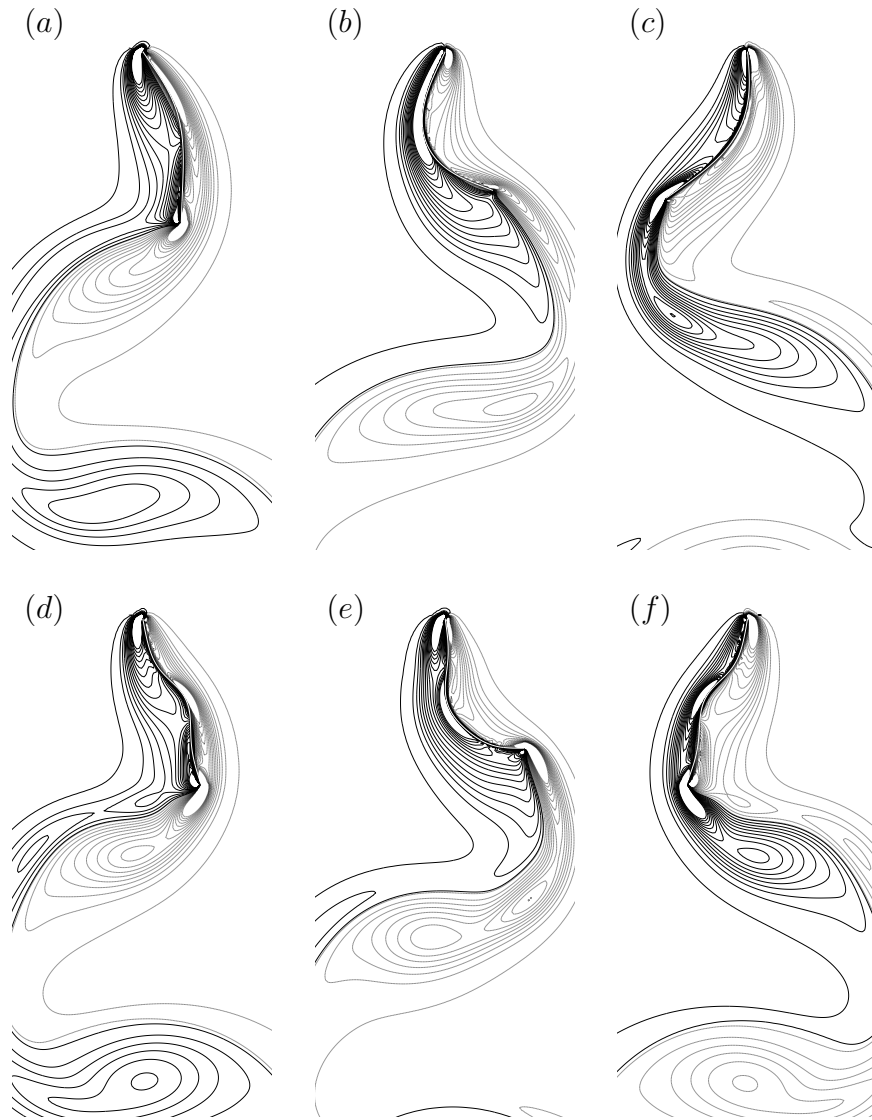


Figure A.13: Vorticity isocontours ($[-15 : 15]$) around impermeable flapping filament ($Re = 200$, $Fr = 0$, positive vorticity in black, negative in gray). With reference to Figure A.10, snapshots (a, b, c) refers to case D ($\rho = 1, \gamma = 2.5 \cdot 10^{-3}$) whereas (d, e, f) refers to case B ($\rho = 1, \gamma = 15 \cdot 10^{-3}$).

For a given value of γ , with respect to impermeable case ($\lambda = 0$), a higher value of ρ (heavier filament) is required for the instability onset. Further, as λ is increased a rapid increase in ρ is found for the instability onset.

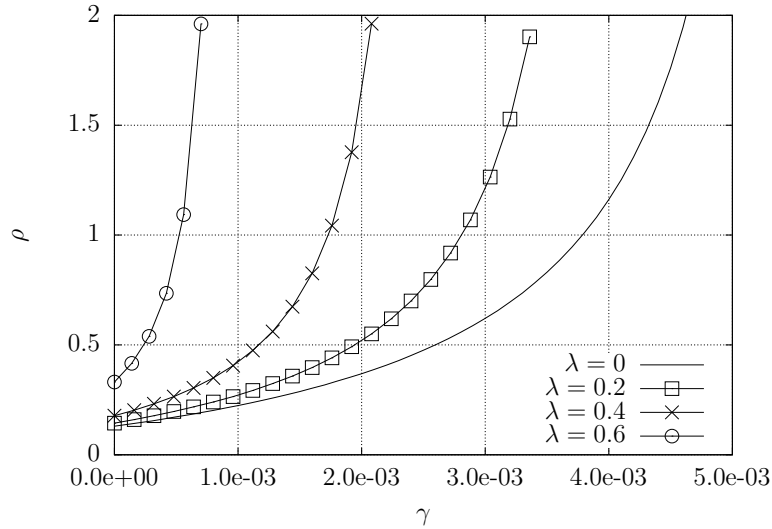


Figure B.14: Neutral curves on the plane (γ, ρ) for $Re = 200$, $Fr = 0$ and different values of the porosity coefficient λ .

References

1. Lundell F, Söderberg LD, Alfredsson PH. Fluid mechanics of paper-making. *Annu Rev Fluid Mech* 2011;**43**:195–217.
2. McKinney W, DeLaurier J. Wingmill: An oscillating-wing windmill. *Journal of Energy* 1981;**5**(2).
3. Boragno C, Festa R, Mazzino A. Elastically bounded flapping wing for energy harvesting. *Applied Physics Letters* 2012;**100**:253906.
4. Orchini A, Mazzino A, Guerrero J, Boragno C. Flapping states of an elastically anchored plate in a uniform flow with applications to energy harvesting by fluid-structure interaction. *Physics of Fluids* 2013;**25**:097105.

5. Favier J, Dauplain A, Basso D, Bottaro A. Passive separation control using a self-adaptive hairy coating. *J Fluid Mech* 2009;**627**:451–483.
6. Lācis U, Brosse N, Ingreneau F, Mazzino A, Lundell F, Kellay H, et al. Passive appendages generate drift through symmetry breaking. *Nature Communications* 2014;**5**:5310.
7. Orchini A, Kellay H, Mazzino A. Galloping instability and control of a rigid pendulum in a flowing soap film. *to appear in J Fluid Struct* 2015; .
8. Peskin CS. The immersed boundary method. *Acta Numerica* 2002; :1–39.
9. Zhu L, Peskin CS. Simulation of a flapping flexible filament in a flowing soap film by the immersed boundary method. *Journal of Computational Physics* 2002;**179**:452–468.
10. Kim Y, Peskin CS. Penalty immersed boundary method for an elastic boundary with mass. *Physics of Fluids* 2007;**19**:053103.
11. Kovacs SJ, McQueen DM, Peskin CS. Modeling cardiac fluid dynamics and diastolic function. *Philos Trans R Soc Lond Ser A* 2001;**359**:1299–1314.
12. Fauci LJ, Peskin CS. A computational model of aquatic animal locomotion. *J Comput Phys* 1988;**77**:85–105.
13. Beyer RP. A computational model of the cochlea using the immersed boundary method. *J Comput Phys* 1992;**98**:145–162.
14. Shelley MJ, Zhang J. Flapping and bending bodies interacting with fluid flows. *Annu Rev Fluid Mech* 2011;**43**:449–465.
15. Rayleigh L. On the instability of jets. In: *Proc. Lond. Math. Soc*; vol. 10. 1879, p. 4–13.
16. Connell BSH, Yue DKP. Flapping dynamics of a flag in a uniform stream. *J Fluid Mech* 2007;**581**:33–67.
17. Lighthill MJ. Note on the swimming of slender fish. *J Fluid Mech* 2007; **581**:33–67.

18. Coene R. Flutter of slender bodies under axial strain. *Appl Sci Res* 1992;**49**:175–187.
19. Argentina M, Mahadevan L. Fluid-flow-induced flutter of a flag. *Proc N A S* 2005;**102**(6):1829–1834.
20. Skotheim JM, Mahadevan L. Dynamics of poroelastic filaments. *Proc R Soc Lond A* 2004;**460**:1995–2020.
21. Uhlmann M. An immersed boundary method with direct forcing for the simulation of particulate flows. *Journal of Computational Physics* 2005;**209**(2):448–476.
22. Pinelli A, Naqavi IZ, Piomelli U, Favier J. Immersed-boundary methods for general finite-difference and finite-volume navier-stokes solvers. *Journal of Computational Physics* 2010;**229**(24):9073–9091.
23. Favier J, Revell A, Pinelli A. A lattice boltzmann-immersed boundary method to simulate the fluid interaction with moving and slender flexible objects. *Journal of Computational Physics* 2014;**261**:145–161.
24. Huang WX, Shin SJ, Sung HJ. Simulation of flexible filaments in a uniform flow by the immersed boundary method. *Journal of Computational Physics* 2007;**226**:2206–2228.
25. Kim Y, Peskin CS. 2-d parachute simulation by the immersed boundary method. *SIAM Journal on Scientific Computing* 2006;**28**(6):2294–2312.
26. Wexler JS, Trinh PH, Berthet H, Quennouz N, du Roure O, Huppert HE, et al. Bending of elastic fibres in viscous flows: the influence of confinement. *J Fluid Mech* 2013;**720**:517–544.
27. Goldstein D, Handler R, Sirovich L. Modeling a no-slip flow boundary with an external force field. *Journal of Computational Physics* 1993;**105**:354–366.
28. Roma AM, Peskin CS, Berger MJ. An adaptive version of the immersed boundary method. *Journal of Computational Physics* 1999;**153**:509–534.
29. Chorin AJ. Numerical solution of the Navier-Stokes Equations. *Math Comp* 1968;**22**:745–762.

30. Temam R. Une méthode d'approximation des solutions des équations Navier-Stokes. *Bull Soc Math France* 1968;**98**:115–152.
31. Perot JB. An analysis of the Fractional Step Method. *Journal of Computational Physics* 1993;**108**:51–58.
32. Munk MM. The aerodynamic forces on airship hulls. *NACA Reports* 1924;**184**.
33. Bagheri S, Mazzino A, Bottaro A. Spontaneous symmetry breaking of a hinged flapping filament generates lift. *Physical Review Letters* 2012; **109**:154502.
34. Procaccia I, L'vov VS, Benzi R. Theory of drag reduction by polymer in wall-bounded turbulence. *Rev Mod Phys* 2008;**80**:225–247.
35. Kellay H, Wu X, Goldberg WI. Experiments with turbulent soap films. *Phys Rev Lett* 1995;**74**:3975–3978.